Progress in Organic Coatings 215 (2026) 110140

Contents lists available at ScienceDirect

Progress in Organic Coatings

journal homepage: www.elsevier.com/locate/porgcoat

Integrating passive radiative cooling with robust superhydrophobicity in hierarchically structured PDMS films using synergistic h-BN/SiO_2

Xinyu Chen [a], Qingyun Zhao [a], Nan Zhang [a], Yanping Yuan [a], Shady Attia [b], Zhaoli Zhang [a,*]

[a] School of Mechanical Engineering, Southwest Jiaotong University, Chengdu, 610031, China
[b] Sustainable Building Design Lab, Dept. UEE, Faculty of Applied Sciences, University of Liège, Liège, 4000, Belgium

ARTICLE INFO

Keywords:
Radiative cooling
Polydimethylsiloxane
Inorganic particles
Superhydrophobicity
Energy conservation

ABSTRACT

Passive radiative cooling (RC) has emerged as a promising energy-free cooling strategy to mitigate the adverse energy and environment impacts of conventional mechanical cooling technology. However, practical application of the conventional polydimethylsiloxane (PDMS) based RC film is largely limited by the insufficient cooling performance and limited self-cleaning ability. This paper proposes a PDMS-based RC composite film via tape-casting, incorporating hexagonal boron nitride (h-BN) and silicon dioxide (SiO_2) as functional fillers to enhance the RC performance. A rough surface microstructure is further constructed on the film using a spray method to realize superhydrophobicity and self-cleaning functionality. Results indicate that the PDMS RC film exhibits noticeable wide band spectrum modulation: a solar reflectance of 93.2% (95.6% in the visible spectrum) and an atmospheric window emissivity of 92.3%. A sub-ambient temperature reduction of 19.4 °C is determined under 886.0 W/m^2 solar irradiance. The enhanced RC performance is attributed to the high solar reflectance enabled by the high refractive index of h-BN and the strong mid-infrared emissivity arising from Si—O bond vibrations in SiO_2. Furthermore, the roughened surface and hydrophobic inorganic particles impart excellent superhydrophobicity to the as-prepared RC film, achieving a water contact angle up to 172.3°. The as-prepared RC film reveals robust performance, maintaining its superhydrophobicity after 10 abrasion cycles and contamination exposure to common liquids, along with excellent mechanical stability during flexibility and load tests. In conclusion, this study designs a PDMS based RC composite film with facile fabrication, mechanical stability and excellent RC performance, offering a feasible solution for energy conservation and climate mitigation.

1. Introduction

Building energy consumption represents an important challenge in the energy field. It occupies more than one-third of the total global energy consumption [1]. Conventional vapor-compression air conditioning systems rely on electricity for operation, accounting for approximately 16% of the total building electricity consumption [2]. This sight also significantly contributes to the urban carbon emission. Thus, many investigations have focused on near-zero energy cooling technologies suitable to building energy conservation. Passive RC is an emerging cooling approach without additional energy input. It achieves cooling by emitting thermal radiation through the atmospheric window (8–13 μm) to the deep cold space (≈3 K), while efficiently reflecting the solar radiation (0.3–2.5 μm) [3]. The combination of two mechanisms enables the full spectrum regulation of thermal radiation, providing passive cooling performance across day-night cycles.

Remarkable achievements have been obtained in passive RC technology, with numerous studies reporting sub-ambient cooling performance during the daytime [4–8]. Materials for RC, including photonic crystals, polymer films and bio-derived fibers, have emerged in recent years [9]. However, photonic crystals (e.g., Poly(St-MMA-AA) and PS) suffer from mechanical rigidity and energy-intensive nanofabrication requirements [10]. Bio-derived fiber RC materials (e.g., cellulose and chitin) generally face challenges related to structural robustness and long-term stability under harsh outdoor conditions [11]. Polymers are widely regarded as low-cost and easily processable materials suitable for scalable applications. Polydimethylsiloxane (PDMS) is an ideal flexible substrate due to its excellent thermal and chemical stability. Its Si-O-Si bonds and amorphous structure impart near-blackbody infrared emissivity. It enables efficient thermal radiation in the atmospheric window and is prevalent in RC applications [12–17]. Whereas, PDMS transmits over 90% visible light, resulting in low reflectance and excessive solar

* Corresponding author.
E-mail address: zzlyzhang@outlook.com (Z. Zhang).

https://doi.org/10.1016/j.porgcoat.2026.110140
Received 28 January 2026; Received in revised form 16 March 2026; Accepted 23 March 2026

heat absorption. Various additives (metals, polymers, and inorganic particles, etc.) are introduced into PDMS to mitigate absorption performance [18–21]. Compared with metals and polymeric addition, inorganic particles offer advantages in terms of facile processing and cost-effectiveness [22]. In particular, the unique 2D shape and high refractive index of hexagonal boron nitride (h-BN) yields an ultra-high backward light scattering efficiency for enabling high solar reflectance [23]. Furthermore, h-BN can excite phonon-polaron resonance in the mid-infrared range, which contributes to high intensity and directional thermal radiation [24]. Yan et al. [25] reported a solar reflectance of 80.9% and a thermal emissivity of 91.3% in h-BN doped nanocomposites. Zhang et al. [26] prepared a composite material using h-BN, achieving a solar reflectance exceeding 86% and an emissivity above 93%, which can reduce substrate temperature. Silicon dioxide (SiO_2) is another widely used inorganic filler due to its low extinction coefficient and strong infrared emission capability. SiO_2 particles effectively enhance the infrared emissivity within the atmospheric window, while exhibiting minimal solar absorption, thereby improving overall RC performance. Yalçın et al. [27] demonstrated highly efficient RC by exploiting the scattering and high emissivity properties of SiO_2. Zhang et al. [28] prepared RC fabrics via in situ synthesis of SiO_2. Depending on solar reflectance of 70.0% and atmospheric window emissivity of 95.0%, it achieved a maximum temperature reduction of 11.2 °C. In addition, other inorganic particles (TiO_2, ZrO_2, etc.) also have been reported to add into the PDMS substrate. Admirable improvement can be found both in solar reflectance and infrared thermal emissivity of composite films [29,30]. Overall, single-particle incorporation has proven to be effective in enhancing either the solar reflectance or infrared emissivity of RC materials.

However, current single-particle incorporation is generally insufficient to simultaneously optimize solar reflection and infrared emission, which can substantially compromise daytime RC performance. According to Mie scattering theory, scattering efficiency depends on the matching of wavelength and particle size [31], a single particle size cannot effectively cover the entire spectrum. Consequently, dual-particle doping enables multi-scale scattering over a broader wavelength range and thus offers a viable strategy for balanced spectral regulation. Recent studies have demonstrated the effectiveness of binary-particle designs. Bao et al. [32] reported a TiO_2/SiO_2 coating with a solar reflectance of 90.7% and an atmospheric window emissivity of 90.1%. Maximum temperature drops of 17.0 °C and 5.0 °C were established during daytime and nighttime, respectively. Feng et al. [33] developed a ZrO_2/TiO_2 double-layer coating, achieving a solar reflectance of 92.9% and an atmospheric window emissivity of 95.1%. Ran et al. [34] achieved a solar reflectance of 90% and a mid-infrared emissivity of 93% by incorporating h-BN and lithium bromide (LiBr) into a radiative evaporative cooling film. Xia et al. [35] enhanced Mie scattering by introducing SiO_2 and TiO_2 particles with different sizes into polyvinylidene difluoride (PVDF), yielding a solar reflectance of 91.16% and an atmospheric window emissivity of 91.41%. Zhang et al. [36] prepared coatings by in-situ growth of BN nanosheets on hollow SiO_2 spheres, achieving 80% solar reflectance and 85% infrared emissivity. These aforementioned studies indicate that dual-particle systems with complementary optical responses are more effective for full-spectrum radiative regulation than single-particle designs.

Besides the spectrum modulation of solar radiation and atmospheric window, the long-term stability of composite RC films is essential to expand their practical deployment. Contaminants (e.g., dusts, particles, liquids) inevitably accumulate on the surface of the RC materials, adversely affecting solar reflectance and infrared emissivity and ultimately degrading cooling performance. Superhydrophobicity is essential to maintain long-term cooling efficiency of RC films, as it enables self-cleaning by automatically removing surface contaminants. This can be effectively realized by constructing hierarchical micro-nano surface roughness. The rough structures form an air layer beneath water droplets, reducing solid-liquid contact and facilitating droplet roll-off, thereby achieving self-cleaning performance. It is perceived that the rough surfaces can be constructed by available methods such as the template [37,38] and spray method [39,40], etc. The spray method is particularly advantageous, allowing for direct and rapid coverage of complex 3D geometries without the intricate molds. Zhao et al. [41] employed PDMS as a superhydrophobic agent deposited via spraying, achieving a water contact angle exceeding 150.0°. Similarly, He et al. [42] fabricated a PDMS/SiO_2 coating using the spray method, which turns out to maintain a contact angle above 150.0°. Xu et al. [43] reported a superhydrophobic polytetrafluoroethylene (PTFE)/PVDF RC coating. This coating exhibited excellent performance metrics: a water contact angle of 153.7°, along with a solar reflectance of 93.7% and an infrared emissivity of 93.3%. Collectively, the spray method provides an effective and scalable route to constructing rough superhydrophobic surfaces with strong self-cleaning capability. The improved hydrophobicity enables long-term retention of solar reflectance and infrared emissivity, ensuring stable RC performance in outdoor environments.

Based on the above reviews, dual-particle strategies have shown promise in enhancing the optical performance of RC materials. However, a systematic understanding of how dual-particle incorporation collectively modulates solar reflectance and infrared emissivity across the full spectrum is still lacking. In addition, most reported PDMS-based composite films exhibit limited water contact angles, resulting in poor self-cleaning ability and vulnerability to fouling in humid or rainy environments. Accordingly, integrated strategies that simultaneously address spectral regulation and surface hydrophobicity in dual-particle RC systems remain underexplored. In this study, an integrated tape casting-spraying strategy is employed to fabricate PDMS-based RC films. High reflectance h-BN and high emissivity SiO_2 are incorporated into the PDMS substrate as functional fillers via the tape casting. A simple spray method is subsequently used to construct a roughened surface composed of homogeneous materials (PDMS, h-BN, SiO_2), ensuring superior material compatibility and structural stability. By incorporating h-BN and SiO_2 with complementary optical properties, the spectral properties of the RC films can be synergistically regulated, leading to a significant enhancement in RC performance. The effects of filler content, film thickness, and surface spraying amount on the cooling performance are systematically investigated. This paper further evaluates the cooling performance of RC films under various real-world scenarios and the durability against various environmental stressors. These obtained results are expected to facilitate the optimal design of high-performance PDMS-based (PBNS) RC films.

2. Experimental

2.1. Materials

PDMS (including PDMS elastic precursor part A and Sylgard184 silicone rubber curing agent part B) was purchased from Dow Corning (USA). h-BN particles (particle sizes of 20 nm) were purchased from Hebei Muyu New Material Co., Ltd. (China). SiO_2 particles (particle sizes of 30 nm) were purchased from Chengdu Kelong Chemical Co., Ltd. (China). Ethyl acetate ($C_4H_8O_2$) was purchased from Chengdu Cologne Chemical Co., Ltd. (China).

2.2. RC film fabrication

2.2.1. Fabrication of PBNS RC film

The PDMS RC film doped with dual inorganic particles of h-BN and SiO_2 was prepared through a tape casting method, as illustrated in Fig. 1. h-BN and SiO_2 particles firstly experienced ball milling at various mass ratios to rapidly mix. PDMS (Part A and Part B), ethyl acetate and premixed inorganic particles were then mixed at a mass ratio of 10:1:4:3, and magnetically stirred for 2 h, forming a homogeneous solution system (solution A) at room temperature. The solution A was further poured into a PTFE mold that was maintained to level naturally. It was

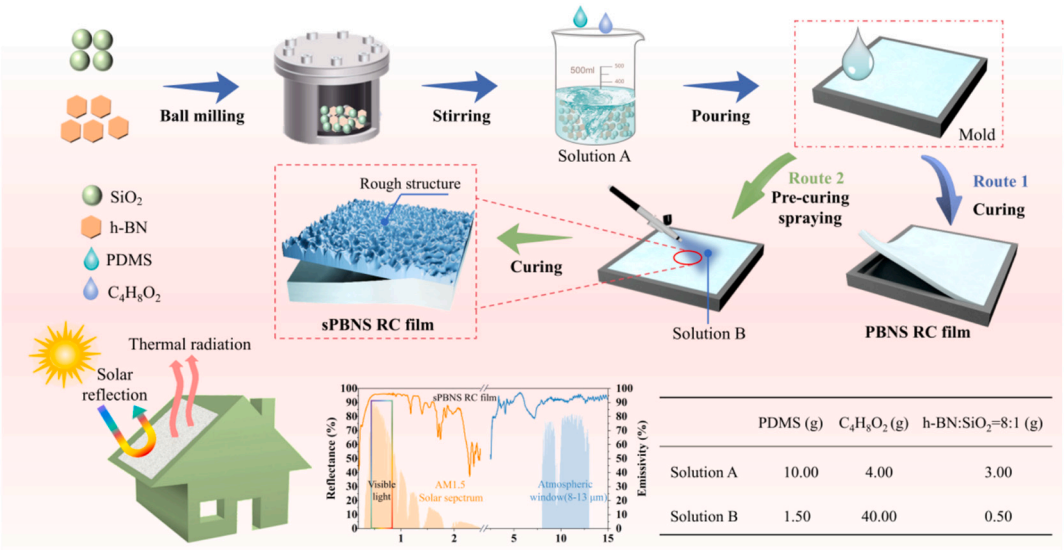

Fig. 1. Schematic of PDMS based RC films preparation.

pre-cured at low temperature of 35.0 °C for 8 h, followed by being cured at high temperature of 70.0 °C for 8 h in an oven. The PDMS/h-BN/SiO_2 (PBNS) RC film was obtained by peeled off the mold once it is completely cooled to room temperature.

2.2.2. Fabrication of sPBNS RC film

In order to increase hydrophobicity of the PBNS RC film, the surface roughness structure was constructed by a spraying method. The uncured film prepared based on a tape casting method as described in Section 2.2.1 firstly experienced low temperature pre-curing for 10 min, in order to obtain a semi-cured PBNS RC film with improved adhesion. Partial PDMS/h-BN/SiO_2 dispersion (solution B) in various proportions (Table 1) was then uniformly deposited onto the surface of the semi-cured PBNS RC film vis the spraying method. After that, the sample was then successively cured for 8 h in a 70.0 °C oven, ultimately producing a superhydrophobic PBNS RC film (sPBNS RC film).

2.3. Structural and morphology characterization

The microstructure of the RC film was observed by a field emission scanning electron microscope (Sigma 500, ZEISS, Germany) at an accelerating voltage of 15 KV. The element distribution was analyzed using an energy dispersive X-ray spectrometer (EDS) at a working voltage of 20 KV to observe the dispersion of particles. An X-ray diffractometry (XRD, Malvern Panalytical, England) was used to test the crystal structure of the film at a scanning angle of 10° to 80°. A thermogravimetric analyzer (TGA/DSC3+, Mettler-Toledo, Switzerland) was used to measure the thermogravimetric curves of the film under a nitrogen atmosphere at a temperature range of 30.0 °C to 800.0 °C and a heating rate of 10 °C/min. The chemical structures of the film were tested by a Fourier transform infrared (FTIR) spectrometer (Nicolet iS50, Thermo Fisher Scientific, USA). The water contact angle (WCA) of the RC film was detected with a 25 μL water droplet at room temperature using a contact angle meter (SINDIN, SDC100, China). The average of five different positions per sample was taken as the measurement result.

Table 1
Ingredients of solution B in sPBNS RC preparation.

Type	PDMS (g)	$C_4H_8O_2$ (g)	h-BN:SiO_2 = 8:1 (g)
SP1	0.50	13.33	0.17
SP2	1.00	26.67	0.33
SP3	1.50	40.00	0.50

2.4. Spectral test

In diffuse reflectance mode, reflectance spectra of the RC films in the wavelength range of 0.25–2.5 μm were recorded by a UV-VIS-NIR spectrophotometer (U-4100, Hitachi, Japan) equipped with an integrating sphere. Absorption spectra within the atmospheric window range (8–13 μm) were acquired using an FTIR spectrometer coupled to an integrating sphere in diffuse reflection mode. The average reflectance ($\overline{R}_{solar}$) and emissivity ($\overline{\varepsilon}_{LWIR}$) were subsequently calculated through the following formulas [44]:

$$\overline{R}_{solar} = \frac{\int_{0.25\ \mu m}^{2.5\ \mu m} I_{solar}(\lambda) \times R_{solar}(\lambda,\theta) d\lambda}{\int_{0.25\ \mu m}^{2.5\ \mu m} I_{solar}(\lambda) d\lambda} \quad (1)$$

$$\overline{\varepsilon}_{LWIR} = \frac{\int_{8\ \mu m}^{13\ \mu m} I_{BB}(T,\lambda) \times \varepsilon_{LWIR}(T,\lambda) d\lambda}{\int_{8\ \mu m}^{13\ \mu m} I_{BB}(T,\lambda) d\lambda} \quad (2)$$

$$I_{BB}(T,\lambda) = \frac{2\,hc^2}{\lambda^5} \frac{1}{e^{\frac{hc}{(\lambda k_B T)}} - 1} \quad (3)$$

where λ is the wavelength of incident light in the range 0.25–2.5 μm; θ is the angle of incidence of light; I_{solar} is the ASTM G173 global solar intensity spectrum; $R_{solar}(\lambda,\theta)$ is the angular spectral reflectance of the surface; $I_{BB}(T,\lambda)$ is the emissivity spectra of a blackbody at 25.0 °C and $\overline{\varepsilon}_{LWIR}$ is the spectral hemispherical thermal emissivity of the surface in long wave infrared (LWIR); h is the Plank constant; k_B is the Boltzmann constant; c is the speed of light in vacuum; λ is the wavelength.

2.5. Theoretical calculation of the cooling power

Theoretically, the cooling power $P_{cool}(T)$ is equivalent to the blackbody radiation subtracted by thermal radiation with the atmosphere, solar irradiation, and heat exchange channels through conduction and convection [45]:

$$P_{cool}(T) = P_{rad}(T) - P_{atm}(T_{amb}) - P_{sun} - P_{cc}(T, T_{amb}) \quad (4)$$

where $P_{rad}(T)$ is the power radiated by the RC film; $P_{atm}(T_{amb})$ is the power of the incident atmospheric radiation by atmospheric heat exchange outside the atmospheric window region; P_{sun} is the absorbed incident power from the sun; $P_{cc}(T, T_{amb})$ is the conduction and convection power; T is the temperature of the RC film, and T_{amb} is ambient

temperature.

The radiated power $P_{rad}(T)$ denotes the power that can be radiated by the RC film in the entire spectrum range [45]:

$$P_{rad}(T) = A\int d\Omega\cos\theta\int_0^{\infty} d\lambda I_{BB}(T,\lambda)\varepsilon(\lambda,\theta) \quad (5)$$

where A is the surface area of the RC film; λ is the wavelength; θ is the angle between the direction of the steradian angle and the direction normal to the surface; $\int d\Omega = 2\pi\int_0^{\pi/2}\sin\theta d\theta$ is the angular integral over the hemisphere; $\varepsilon(\lambda,\theta)$ is the spectral angular emissivity of the surface.

The incident atmospheric cooling power $P_{atm}(T_{amb})$ outside the atmospheric window region, arising from atmospheric heat exchange is given by [45]:

$$P_{atm}(T_{amb}) = \int\int_0^{\infty} I_{BB}(T_{amb},\lambda)\varepsilon(\lambda,\theta)\varepsilon_{atm}(\lambda,\theta)d\lambda\cos\theta d\Omega \quad (6)$$

where $\varepsilon_{atm}(\lambda,\theta) = 1 - t(\lambda)^{1/\cos\theta}$ and $t(\lambda)$ are the atmospheric emissivity and the atmospheric transmittance in the zenith direction, respectively.

The absorbed incident cooling power from the sun P_{sun} can be expressed as [45]:

$$P_{sun} = A\int_0^{\infty} d\lambda\varepsilon(\lambda,\theta_{sun})I_{AM1.5}(\lambda) \quad (7)$$

where $I_{AM1.5}$ is the solar illumination intensity.

According to the Newton's law of cooling, the combined conduction and convection cooling power $P_{cc}(T,T_{amb})$ can be calculated as [45]:

$$P_{cc}(T,T_{amb}) = Ah_{cc}(T_{amb} - T) \quad (8)$$

where h_{cc} the convective coefficient of the nonradiative transfer, including heat conduction and convection.

2.6. Self-cleaning and mechanical stability tests

Self-cleaning performance was assessed by spreading several contaminants (sand, $CuSO_4{\cdot}5H_2O$, graphite powder, glycerol) on the surface of the RC film to simulate contamination, followed by flushing with the deionized water. The contaminant removal process was recorded by a digital camera. Anti-fouling performance was assessed by dripping common liquid contaminants (tea, milk, ink, coffee, water, juice). The acid/alkaline tolerance of the film was evaluated by immersing it in solutions with different pH values and measuring the contact angle. The film was exposed to a spray environment for an extended period to simulate rainwater erosion. Mechanical stability was evaluated by laying the superhydrophobic side of the film on a 120-mesh filter horizontal screen. A 500 g weight was placed on the top non-superhydrophobic side. The film was pushed parallel to a ruler under an external force, with a 10 cm displacement defined as one friction cycle. The contact angle of the RC film surface was measured after each cycle. When it comes to the evaluation of the mechanical stability, film was subjected to bending, torsion and uniaxial tensile tests under different loads. The deformation ability and structural recovery ability of the film were subsequently detected in these tests.

3. Results and discussion

3.1. Structure and morphology

Fig. 2(a) exhibits that the PBNS RC film manifests a white

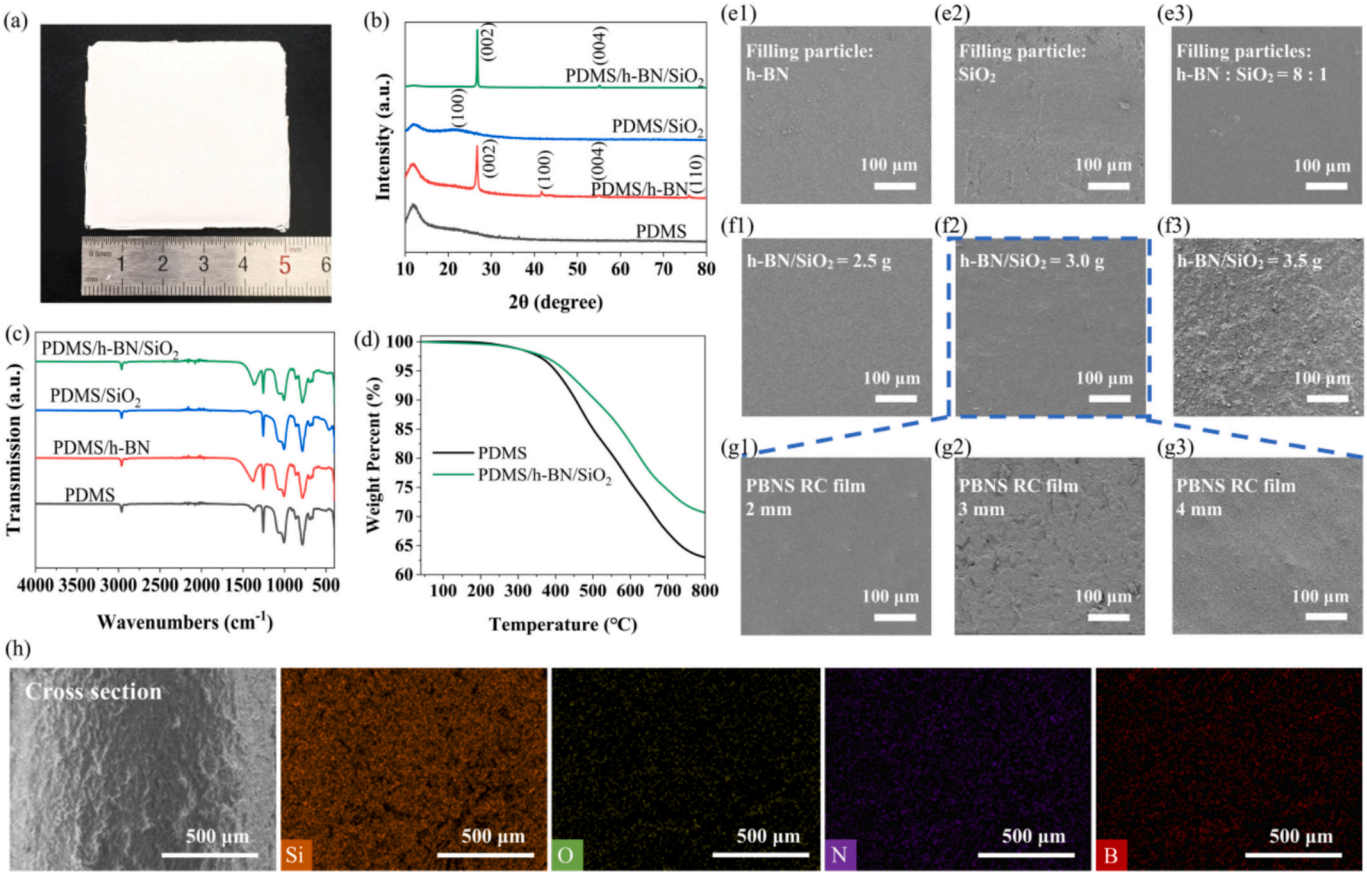

Fig. 2. Structure and morphology of the PBNS RC film. (a) Apparent morphology; (b)XRD spectrum; (c) FTIR spectrum; (d) TGA curves; (e1–g3) SEM images; (h) EDS images.

appearance, which is attributable to light scattering by h-BN and SiO_2 particles. The XRD spectrum (Fig. 2(b)) displays a characteristic peak at 20.9°, corresponding to the unique crystal plane (100) plane of SiO_2. The characteristic peaks appearing at 26.7° (002), 41.6° (100), 55.1° (004), and 76.0° (110) reflect typical diffraction of a hexagonal crystal structure for h-BN. The finding identifies that the crystallographic structure and composition of h-BN and SiO_2 particles are reserved in during fabrication process of the PBNS RC film. The FTIR spectrum of PDMS, h-BN, SiO_2, and the PBNS RC films are compared in Fig. 2(c). No new absorption peaks appeared theoretically indicates absence of chemical reaction. Meanwhile, PDMS and PBNS RC film contains various stretching vibration peaks located in the range of 1257–783 cm^{-1} that is precisely corresponding to the atmospheric window. TGA analysis depicted in Fig. 2(d) was conducted to evaluate the thermal stability of RC films. It is elaborated that the thermal decomposition behavior of both films is similar between 0 and 300 °C. After that, the PBNS RC film obtains higher weight percentage than the PDMS film. Difference in weight percentage of two films becomes larger with the temperature rises, reaching approximately 8% at 800 °C. This is attributed to the incorporation of doped h-BN and SiO_2, whose high intrinsic thermal stability and interfacial interactions with the polymer substrate collectively enhance the thermal stability of the film [46].

Fig. 2(e1–g3) presents SEM images of the surface for PBNS RC films. Fig. 2(e1, e2) shows that since the PDMS substrate has admirable compatibility with the h-BN and SiO_2 fillers, the two particles are evenly dispersed within the PDMS to form a compact and stable structure. Fig. 2 (e3) demonstrates that the PBNS RC film maintains good material compatibility when h-BN and SiO_2 are incorporated simultaneously. A further investigation is conducted to analyze the effect of filler content on the PBNS RC film. When the particle loading does not exceed 3.0 g, both h-BN/SiO_2 particles are homogeneously dispersed throughout the PDMS matrix in Fig. 2(f1, f2), resulting in a dense and well-integrated microstructure. Fig. 2(f3) shows that pronounced particle agglomeration occurs when the particle content exceeds 3.0 g. The sight results from van der Waals interactions between particles surpass the interfacial interactions with PDMS, which further promotes agglomeration. Although the enhanced interactions between particles intensify light scattering, excessive particles will elongate the optical path length and cause failure of Mie scattering ultimately. As shown in Fig. 2(g1–g3), the effect of film thickness on the PBNS RC film structure was also examined. The particle dispersion deteriorates as the film thickness increases, and that evidently alters the surface morphology of the PBNS RC films. This phenomenon mainly arises from two mechanisms: (1) Thicker film leads to gradient evaporation of solvent and internal convection during curing, which promotes the migration and clustering of inorganic particles; (2) Thicker films causes inhomogeneity of the photo-polymerization reaction, generating the local cross-linking density variations and uneven distribution of particles [47]. Fig. 2(h) shows that, the elemental mapping demonstrates that the characteristic elements of B, N, Si, and O are uniformly distributed throughout the composite film. This result further confirms the homogeneous dispersion of the fillers in the PDMS matrix.

3.2. Spectral properties and binary synergistic mechanism

Fig. 3 depicts the optical constants (refractive index (n) and extinction coefficient (k)), reflectance, and emissivity of the prepared PBNS RC films. The ideal RC films are expected to possess both high solar reflectance in the solar spectrum and high emissivity in the atmospheric window to enable efficient cooling. Films with a high n and a low k have been reported to generally exhibit high solar reflectance. Fig. 3(a–c) shows the optical constants of h-BN, PDMS, SiO_2. h-BN possesses a high refractive index ($n > 2.2$) [48] and a near-zero extinction coefficient across the visible to near-infrared spectrum. This configuration can effectively reflect solar radiation to reduce solar energy absorption, reestablishing the regulation of the light propagation path. The low refractive index of PDMS (n ~ 1.4) forms pronounced refractive index contrast with the embedded fillers. Such interfacial contrast promotes light scattering and enhances solar reflectance [49]. Furthermore, SiO_2 exhibits a low extinction coefficient owing to its wide band-gap [50], while the vibrational absorption of Si—O bonds significantly boosts emissivity of the RC film.

The as-prepared PDMS-based RC film embedded with h-BN/SiO_2 particles exhibits a synergistic effect of highly efficient solar reflection and selective infrared emission. Fig. 3(d, e) reveal that the reflectance of the PDMS film is notably enhanced after filling with inorganic particles. The solar reflectance of the PDMS/h-BN RC film is found to be 90.49%, which is significantly higher than that of PDMS/SiO_2 RC film (25.55%). This is ascribed to the strong reflectance of h-BN within the solar spectrum. Meanwhile, the PDMS/SiO_2 RC film exhibits an emissivity of 94.4% within the atmospheric window, slightly exceeding that of the PDMS/h-BN RC film (93.3%). This observation is mainly due to the infrared emissivity of SiO_2 within the atmospheric window spectrum. At an h-BN/SiO_2 mass ratio of 8, the PBNS RC film achieves a solar reflectance of 90.2% and an infrared emissivity of 93.5%, effectively leveraging the high reflectance of h-BN and the emissivity of SiO_2.

It is found that h-BN dominates the reflectance modulation in solar spectrum. This can be largely explained by the fact that h-BN possesses a wide band-gap (~6 eV) [51]. It lies well above the photon energy of visible and near-infrared light, effectively suppressing electronic transitions and solar absorption. In addition, the mismatch of refractive index among h-BN, SiO_2, and PDMS generates multiple scattering interfaces, enhancing broadband photon scattering. The scattered photons are more likely to escape from the film surface rather than being dissipated as heat, thereby improving solar reflectance. Moreover, SiO_2 exhibits strong Si—O vibrational modes in the mid-infrared region, which facilitates efficient thermal emission within the atmospheric window. Meanwhile, h-BN can excite phonon-polariton resonances in the mid-infrared range, producing lattice vibrational effects and thus exhibiting thermal radiation capability [52]. The co-incorporation of h-BN and SiO_2 promotes coupling of vibrational modes, leading to enhanced emissivity in the 8–13 μm range. Through this binary synergistic mechanism, the PBNS RC film achieves coordinated regulation of solar reflection and mid-infrared emission, thereby enhancing the broad-spectrum optical modulation closely associated with its radiative cooling performance. Furthermore, the low reflectance of the PDMS/SiO_2 film is mainly attributed to the semi-transparent state of that. This semi-transparency allows partial incident sunlight to transmit through the film rather than being completely reflected on the surface, which is adverse to the overall reflectance.

The effect of particle content on optical properties of the PBNS RC films was further investigated. Fig. 3(f, g) releases that the PBNS RC films with varying particle contents all exhibit excellent optical properties. The uniformly dispersed h-BN and SiO_2 particles act as effective light-scattering centers, enhancing reflectance and emissivity through both geometrical and Rayleigh scattering effects [53]. Additionally, solar reflectance increases successively with augment of the filler content. The PBNS RC film containing 3 g of the filler exhibits an exceptional reflectance of 94.0%, which is attributed to the optimized density of the scattering network. Fig. 3(h, i) shows the influence of film thickness on the optical properties of the PBNS RC film. When the thickness falls below the critical threshold (3 mm), both solar reflectance and emissivity of the PBNS RC film rise with increasing thickness. At a thickness of 2 mm, the film achieves a solar reflectance of 94.5% and an infrared emissivity of 93.2%. Further increasing the thickness to 3 mm results in only marginal improvements, with reflectance and emissivity increasing by 0.7% and 0.1%, respectively. This can be explained that the reflection primarily occurs at the air-film interface, whereas the emissivity is related to the absorption depth of bands within the atmospheric window [54]. Moreover, once the film thickness exceeds this critical threshold, both reflectance and emissivity decrease, by 2.3% and 0.7%, respectively, indicating that excessive thickness adversely affects

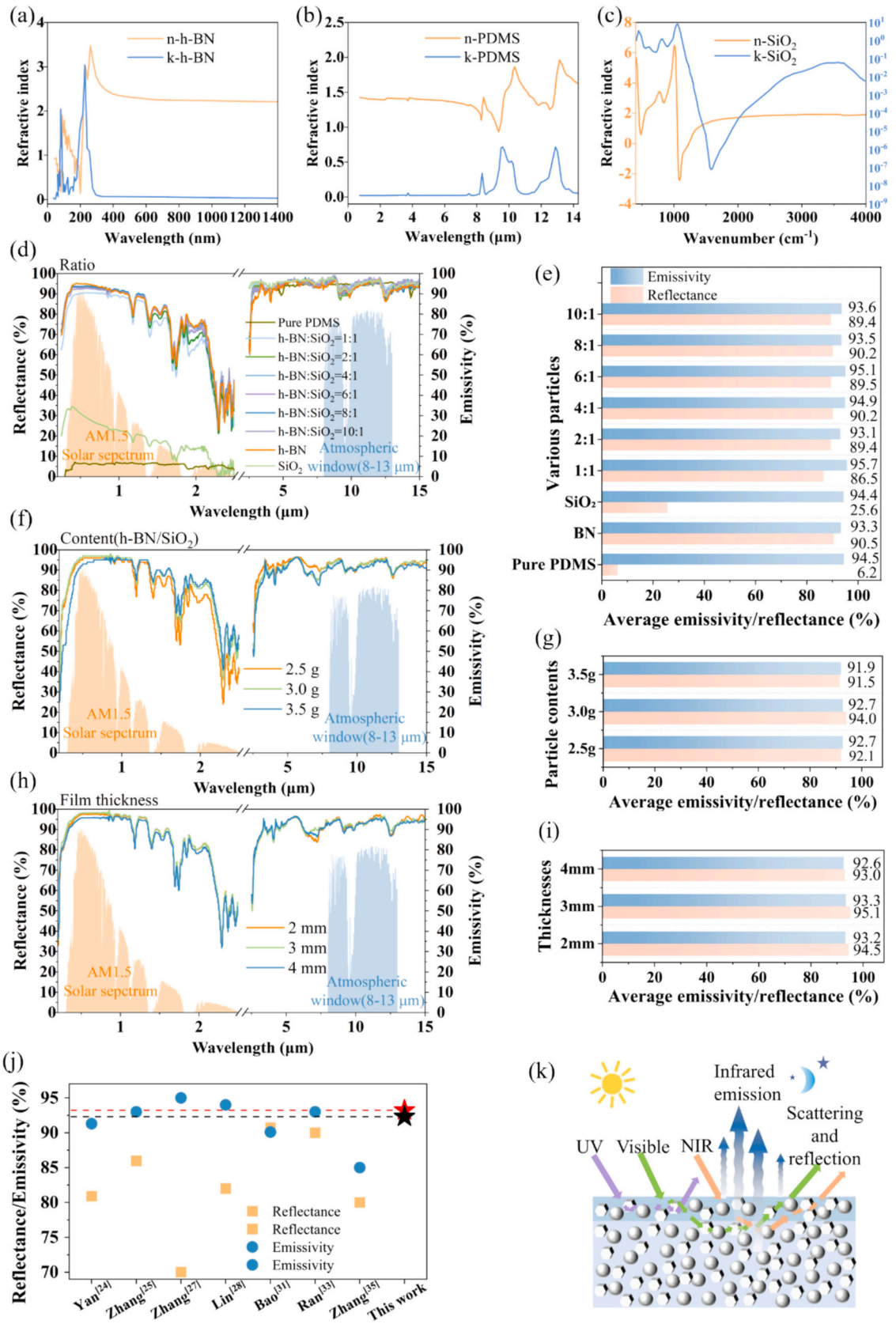

Fig. 3. Spectral properties of the PBNS RC films. (a) The optical constants of h-BN [48]; (b) the optical constants of PDMS [49]; (c) the optical constants of SiO_2 [50]; (d) reflectance and emissivity of the films under various particle ratios; (e) average reflectance and emissivity of the films under various particle ratios; (f) reflectance and emissivity of the films under various particle contents; (g) average reflectance and emissivity of the films under various particle contents; (h) reflectance and emissivity of the films under various film thicknesses; (i) average reflectance and emissivity of the films under various film thicknesses; (j) comparison of reflectance and emissivity in the literatures; (k) RC mechanism.

optical performance. The comparative results in Fig. 3(j) suggests that the synergistic spectral control of film reflectance and emissivity offers a notable advantage over previously reported literatures. Fig. 3(k) illustrates the RC mechanism of the PBNS RC film embedded with binary inorganic fillers. In the UV-VIS-NIR, solar radiation is efficiently reflected and scattered by h-BN and SiO_2, suppressing solar heat gain. In the mid-infrared region, PDMS and SiO_2 exhibit strong emission within the atmospheric window, enabling effective thermal radiation to outer space.

3.3. Cooling performance of the PBNS RC film

A preliminary indoor experiment was conducted to evaluate the RC performance of the PBNS RC films under simulated solar irradiance provided by a xenon lamp (800.0 W/m^2). Fig. 4(a, b) illustrates the experimental device consisting of an expanded polystyrene (EPS) foam box wrapped with aluminum foil for solar reflection. A cavity (50 mm × 50 mm × 10 mm) was created on top to accommodate the test film, while a thermocouple was positioned at the bottom for temperature monitoring. The top of the device is covered with an infrared transparent polyethylene (PE) film to effectively suppress the interference of ambient thermal convection on the test results. Under xenon lamp irradiation, this configuration enables reliable assessment of the RC performance of the PBNS RC films.

Fig. 4(c) shows the cooling performance of PBNS RC films at different h-BN/SiO_2 mass ratios. The excellent cooling effect is obtained when the h-BN/SiO_2 mass ratio is 8. As shown in Fig. 4(d), the RC performance of the PBNS RC film is significantly better than that of the commercial film of the same thickness. The temperature of the PBNS RC film is 14.15 °C lower than that of commercial film, 1.15 °C lower than PDMS/h-BN film, and 5.32 °C lower than PDMS/SiO_2 film. The experimental RC performance verifies that h-BN and SiO_2 function cooperatively to suppress heat gain and promote heat dissipation, leading to enhanced RC compared with single-particle-doped films under identical conditions. The introduction of randomly dispersed h-BN and SiO_2 particles into the PDMS substrate induces scattering, thereby effectively reflecting solar reflection. In the mid-infrared spectrum, the stretching vibrations of Si-O-Si/Si-O and B—N bonds in PDMS, SiO_2, and h-BN, along with phonon polarization, significantly enhance the thermal radiation capacity of the films within the atmospheric window. Meanwhile, SiO_2 possesses a low refractive index, whereas h-BN has a comparatively high refractive index, and their combination establishes a gradient refractive index structure. This structure promotes Mie scattering and multiple optical scattering paths, thereby enhancing broadband reflection and diffuse scattering. Consequently, the film reduces heat accumulation under sunlight and demonstrates superior performance in RC. Based on the study of the indoor RC performance of the PBNS RC film, combined with the effect of synergistic optimization of its reflectance and emissivity, subsequent experiments employed a h-BN/SiO_2 mass ratio of 8:1 as the filler composition.

Fig. 4(e) shows that when the mixed particle content reaches 3.0 g, corresponding to a filler volume fraction of 35.3%, a continuous scattering network is formed within the PBNS RC film. At this condition, the PBNS RC film achieves a good cooling performance, exhibiting a temperature reduction of 8.0 °C compared to the commercial film, together with high solar reflectance. At lower loading levels, inadequate particle dispersion leads to an incomplete scattering network. Conversely, higher loading levels induce optical crowding effects that impair scattering efficiency [55]. The effect of film thickness on the RC performance of the PBNS RC films was further explored at 3.0 g of filled particle content. As shown in Fig. 4(f), the film thickness significantly affects the cooling performance by increasing the optical thickness. At a thickness of 2 mm, the PBNS RC film exhibits a temperature reduction of 8.1 °C compared to the commercial film. The increased thickness can extend the photon propagation path and strengthens light–matter interactions, while suppressing convective heat transfer [56]. However, experimental analysis shows that once the film thickness exceeds 2 mm, further improvements in cooling performance and optical properties become marginal, whereas material consumption and fabrication cost increase noticeably.

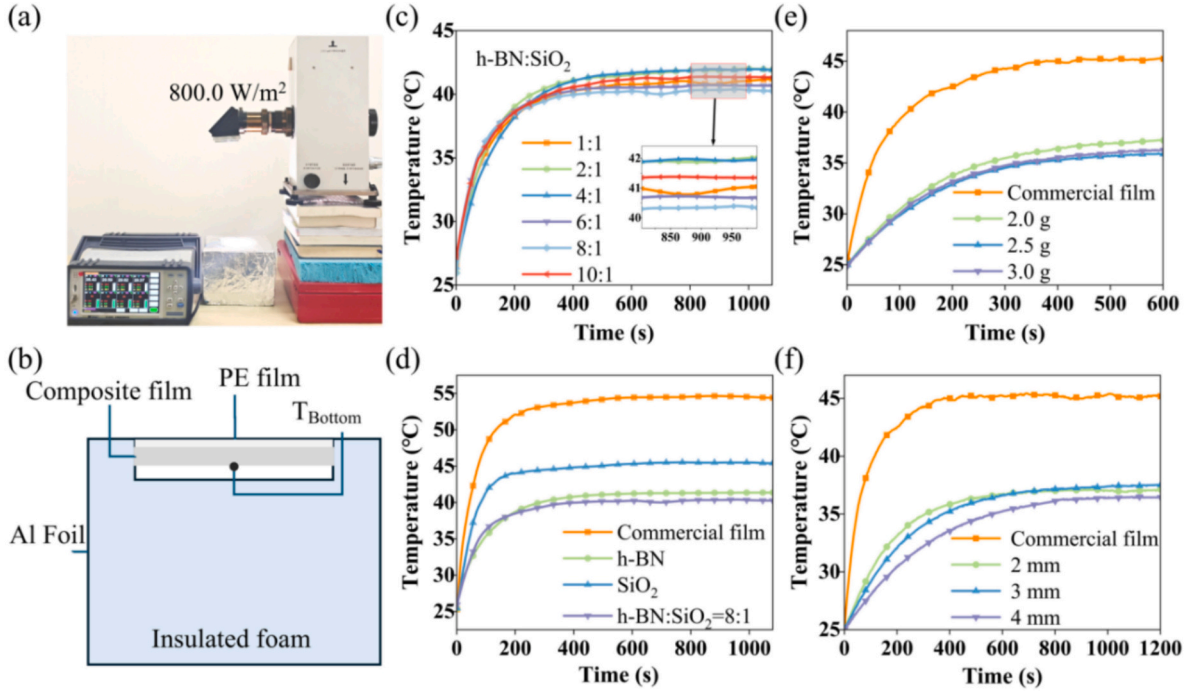

Fig. 4. Results of indoor test. (a) Indoor test; (b) device diagram; (c) temperature variation of the PBNS RC films with different various ratios; (d) temperature variation of the PBNS RC films with various particles; (e) temperature variation of the PBNS RC films with various particle contents; (f) temperature variation of the PBNS RC films with various thicknesses.

3.4. Superhydrophobicity and cooling performance of the sPBNS RC film

When RC films are deployed outdoors, prolonged exposure to moisture and dust inevitably degrades their cooling performance [57]. This thereby reduces reflectance and enhances solar absorption. Constructing a superhydrophobic surface provides an effective strategy to alleviate these issues. In this work, a spray method was adopted to create a rough surface structure on the film, enhancing its hydrophobicity. When spraying onto a semi-cured substrate, fully melted particles form a denser coating with relatively low roughness. In contrast, partially melted particles tended to generate pores and protrusions, resulting in a rougher surface. The spraying solution was prepared according to the formulation listed in Table 1. Under these conditions, the spray solution exhibits good dispersion stability, ensuring uniformity and controllability in film formation. Excessive filler loading causes particle agglomeration and nozzle clogging, compromising film density. Conversely, insufficient filler loading leads to inadequate solution viscosity and poor spraying efficiency, making it difficult to form a continuous and stable film layer. The resulting rough surface increases the proportion of contact between air and water droplets through the alteration of microstructure, thereby raising the contact angle and enhancing the hydrophobicity of the surface [58]. As shown in Fig. 5, the effect of spray amount on the hydrophobicity of the sPBNS RC film, surface morphology, cooling performance, and optical properties was investigated. Fig. 5(a) shows that the water contact angle of the sPBNS RC films increases gradually with increasing spray amount, indicating progressively enhanced surface hydrophobicity. Compared to the unsprayed surface, the contact angle of the sPBNS RC film-SP3 increases by 66.6%. Combined with SEM images in Fig. 5(b), at a spray amount of SP1, the deposited layer is too thin to fully cover the substrate, resulting

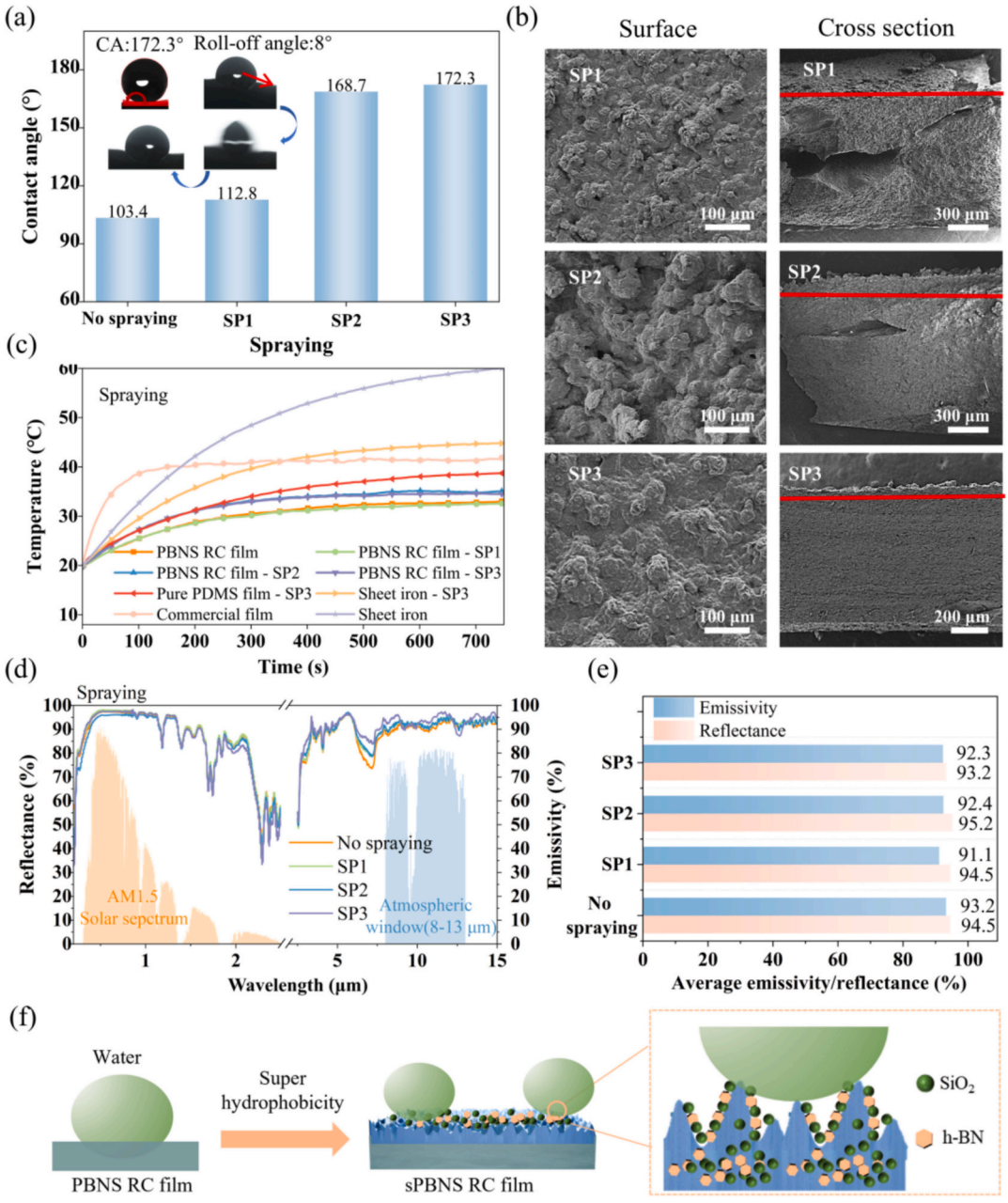

Fig. 5. Test of the effect of spraying on film properties. (a) Contact angle roll-off angle; (b) SEM images; (c) temperature variation of films sprayed on various surfaces; (d) reflectance and emissivity of films under various sprayed on surfaces; (e) average reflectance and emissivity of films under various sprayed on surfaces; (f) schematic of superhydrophobic mechanism.

in a contact angle of only 112.8°. When the spray amount increases to SP2, a well-developed rough microstructure forms on the film surface, raising the contact angle to 168.7°, indicating a significant improvement in hydrophobicity. Further increasing the spray amount to SP3 leads to the formation of hierarchical micro–nano structures. The maximum water contact angle reached 172.3°, with a roll-off angle of 8°, achieving a superhydrophobic state.

Fig. 5(c) shows the xenon lamp test conducted under indoor conditions. Spraying experiments conducted on iron plate demonstrates that the sprayed rough surface exhibits RC properties. This is because the PDMS/h-BN/SiO_2 spray solution exhibits excellent cooling performance, while enlarged the roughened surface radiative area, thereby enhancing heat dissipation. Accordingly, the sPBNS RC film with the spray layer shows good cooling performance. In addition, pronounced Mie scattering can occur when the surface particle size is comparable to the incident wavelength. The rough structure enhances diffuse reflection compared to the specular reflection behavior of a smooth surface. The density of scattering centers rises as the number of surface particles increases, which facilitates the redistribution of photon propagation directions and strengthen of multiple scattering. These effects collectively improve reflectance across the solar spectrum. The radiative transfer equation indicates that the radiative behavior of the film is governed by the absorption coefficient and the scattering coefficient. The spray thickness determines the optical thickness of the film, which affects both the absorption and scattering coefficients. The thin coating generates the low optical thickness, substantially limiting the scattering events. At an appropriate coating thickness, enhanced multiple scattering improves reflectance. In the mid-infrared region, a larger coating

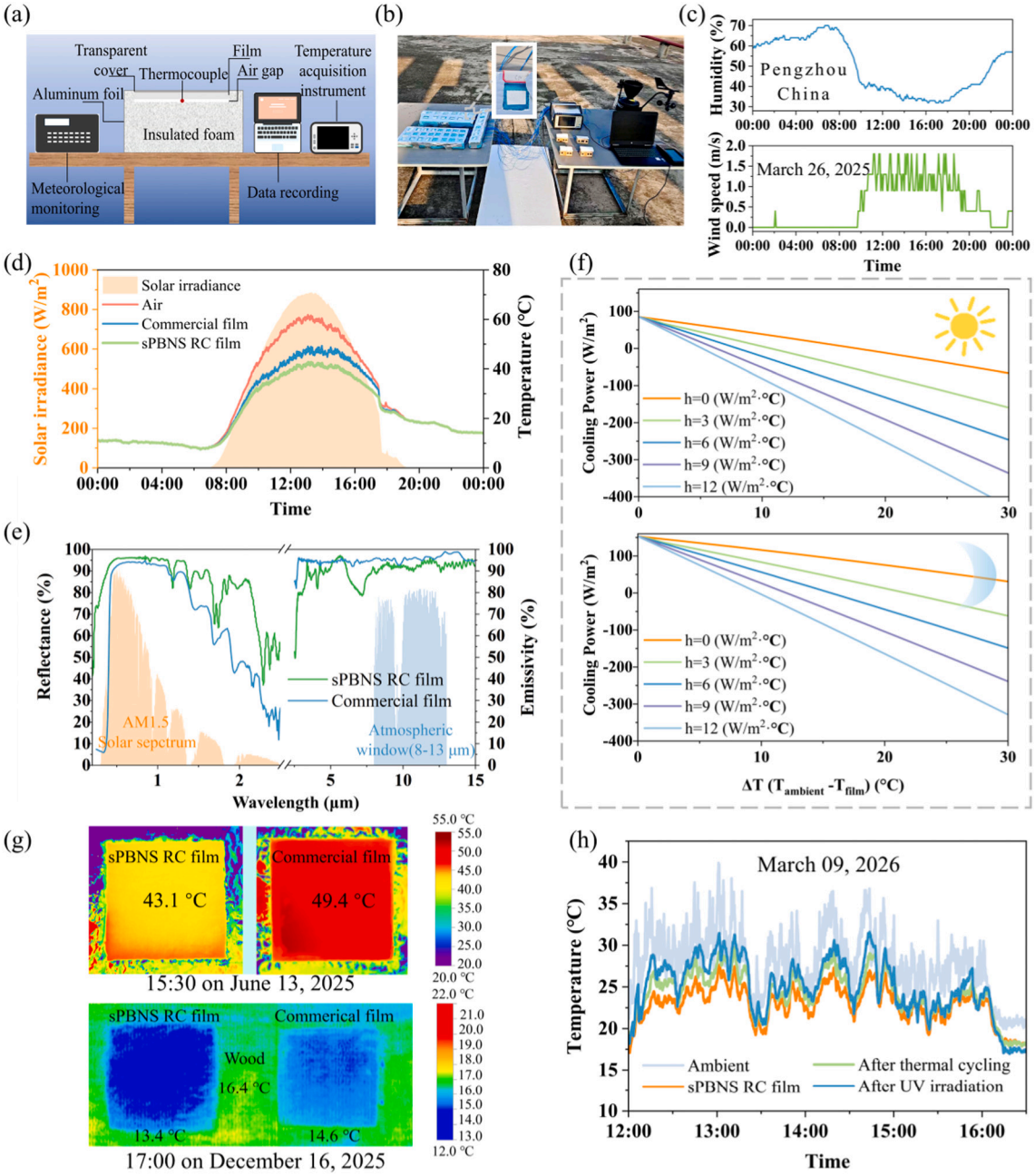

Fig. 6. Results of outdoor field test. (a) Schematic diagram of test; (b) experimental setup of test; (c) weather condition (Pengzhou, China, 2025, 03, 26); (d) daily temperature variation of sPBNS RC films; (e) reflectance and emissivity of the films; (f) theoretical RC power; (g) infrared thermal image; (h) daily temperature variation after UV aging and thermal cycling.

thickness benefits effective absorption. According to Kirchhoff's law, increased absorption corresponds to enhanced emissivity. However, excessive thickness may induce strong multiple scattering, leading to repeated internal radiation within the structure and degraded radiative performance. Compared with the unsprayed film, SP2 and SP3 exhibit slightly reduced RC performance, which is attributed to increased surface irregularities.

Optical characterization in Fig. 5(d, e) reveals that the surface spray amount has a minor effect on the overall reflectance and emissivity of the sPBNS RC films. This is because the spray layer is typically only a few microns thick, accounting for a negligible portion of the optical thickness, and thus contributes minimally to bulk scattering. As the spray amount increases, surface irregularities cause a slight decrease in solar reflectance, while the enhancement in infrared emissivity remains limited. A comprehensive evaluation indicates that the sPBNS RC-SP3 film achieves a well-balanced optimization between hydrophobicity and cooling performance. Although cooling performance slightly decreases, the enhanced superhydrophobicity significantly improves the environmental adaptability of the film. The sPBNS RC film exhibits a solar reflectance of 93.2% (95.6% in the visible spectrum) and an infrared emissivity of 92.3%, confirming its excellent solar radiation management and thermal emission capability. Fig. 5(f) schematically illustrates the mechanism underlying the superhydrophobicity of the sPBNS RC film. The superhydrophobic performance originates from the synergistic effect of two factors. First, micro/nano hierarchical roughness by spraying introduces trapped air at the solid-liquid interface, effectively reducing the contact area between water droplets and the surface. Second, the incorporation of hydrophobic SiO_2 particles lowers the surface free energy, thereby imparting excellent superhydrophobicity to the film.

3.5. Outdoor cooling performance

An outdoor field test was conducted in Pengzhou, China, on March 26, 2025, to evaluate the practical RC performance of the sPBNS RC film. Fig. 6(a, b) shows the schematic and experimental setup of the outdoor test. All the test samples were positioned 1 m above the ground. Their top surfaces were covered with a plastic wrap to suppress convective heat transfer, while the bottom and sides of boxes were insulated with EPS foam to minimize heat dissipation. This configuration ensured the measured temperature changes primarily resulted from net radiation [59]. The experiment was conducted on a rooftop to minimize the effects of thermal radiation and sunlight shading from surrounding buildings. Corresponding weather condition during the test are presented in Fig. 6 (c).

The temperature variation of the sPBNS RC films was recorded throughout the day and night to assess their all-day cooling performance. While the heat accumulation within the enclosure was inevitable, the identical experimental setup ensures that all samples were subjected to a same thermal environment and comparable heat accumulation. Under these controlled conditions, the temperature differences observed among the films can reliably reflect the intrinsic differences in their RC performance. Fig. 6(d) indicates that the daytime temperature of the test sample is consistently lower than that of the reference air and the commercial film. During peak solar irradiance period (12:00–15:00), the sPBNS RC film respectively achieves maximum temperature reductions of 19.4 °C and 7.0 °C, when compared to the reference air temperature and commercial film temperature. This demonstrates that under identical environmental condition, the application of sPBNS RC film significantly suppresses surface temperature rise over no RC film cases. This finding serves to verify the RC regulation capability of the sPBNS RC film.

Theoretically, the cooling performance of the PBNS RC film arises from the synergistic contribution of four mechanisms: (1) Molecular vibrations of the Si-O-Si and Si—O bonds in PDMS and SiO_2 within the mid-infrared region; (2) Reduction of solar absorption due to wide bandgap and refractive index of h-BN; (3) Scattering effect generated by h-BN and SiO_2 filling in PDMS; (4) Diffuse reflection from micro-nano rough structure on the film surface. Fig. 6(e) compares the optical spectra of commercial film and sPBNS RC film. In the solar spectrum, the gradient refractive index design of PDMS and h-BN enhances solar reflectance, thereby suppressing radiative heat gain. The Si—O stretching vibrations of SiO_2 synergistically improve emissivity within the atmospheric window band [60]. Based on atmospheric transmittance data [61], the net RC power of sPBNS RC film under various ambient temperatures (assuming the film temperature is 300 K) was theoretically calculated. Fig. 6(f) illustrates that theoretical daytime RC power of the sPBNS RC film reaches 85.3 W/m^2, while the nighttime RC power increases to 153.0 W/m^2.

The infrared thermal images (15:30 on June 13, 2025) in Fig. 6(g) reveal that the sPBNS RC film maintains a lower temperature than the commercial film (produced by Guangzhou Fumeiao Coatings Co.), which can further confirm its effective cooling performance. The sPBNS RC film and the commercial film were placed on the surface of the wooden board, monitored using an infrared thermal camera. It is observed that both films enable to effectively reduce the surface temperature of the wooden board, indicating their ability to mitigate thermal accumulation. Notably, the sPBNS RC film exhibits superior cooling performance, achieving surface temperatures 1.2 °C and 3.0 °C lower than those of the commercial film and the bare wooden board, respectively. It should be noted that the related absolute temperature decline is substantially confined by the relatively low ambient temperature and limited solar irradiance during the measurement period (17:00 on December 16, 2025). To evaluate long-term durability of the film, ultraviolet aging and thermal cycling tests were conducted in Chengdu, on March 09, 2026. Firstly, the film was exposed to outdoor ultraviolet irradiation for 2 weeks, and the radiative cooling performance before and after UV aging was measured. Secondly, the film was subjected to repeated thermal cycling between 60 °C and − 20 °C, and the cooling performance before and after cycling was evaluated. As shown in Fig. 6 (h), the obtained results indicate that the cooling performance shows only a minimal reduction after UV aging or thermal cycling, while the film still maintains stable radiative cooling capability, demonstrating its excellent environmental stability and durability for long-term outdoor applications.

3.6. Self-cleaning performance

Given that maintenance cost and service life of the sPBNS RC films are closely related to their self-cleaning performance, a superhydrophobic layer was designed to be coated on the surface of the PBNS RC film, and the self-cleaning tests were conducted in this investigation. Simulated contamination tests using several representative contaminants in Fig. 7(a) display the self-cleaning performance of the sPBNS RC film. Specifically, sand was selected to simulate dust particle contaminant in natural environments; $CuSO_4{\cdot}5H_2O$ was used to represent water-soluble inorganic salts remaining after rainwater evaporation; graphite powder was employed to simulate carbonaceous particulate pollution commonly present in urban atmospheres; and glycerol was introduced as a typical organic contaminant in the practical application. The experimental results reveal that the pollutants covered the surface of the film can be effectively removed by rolling water droplets. There are nearly no pollutants remained on the surface of the film after rinsing with water. These findings verify that the fabricated superhydrophobic film exhibits excellent self-cleaning performance under various contamination conditions, highlighting its practical applicability in real outdoor environments. This cleaning performance can be attributed to two aspects: (1) The superhydrophobicity of the sPBNS RC film promotes the rolling motion of water drops rather than their retention on the surface; (2) The affinity between contaminants and water is greater than that between contaminants and the film [62,63]. The low surface energy further suppresses contaminant adhesion, facilitating self-

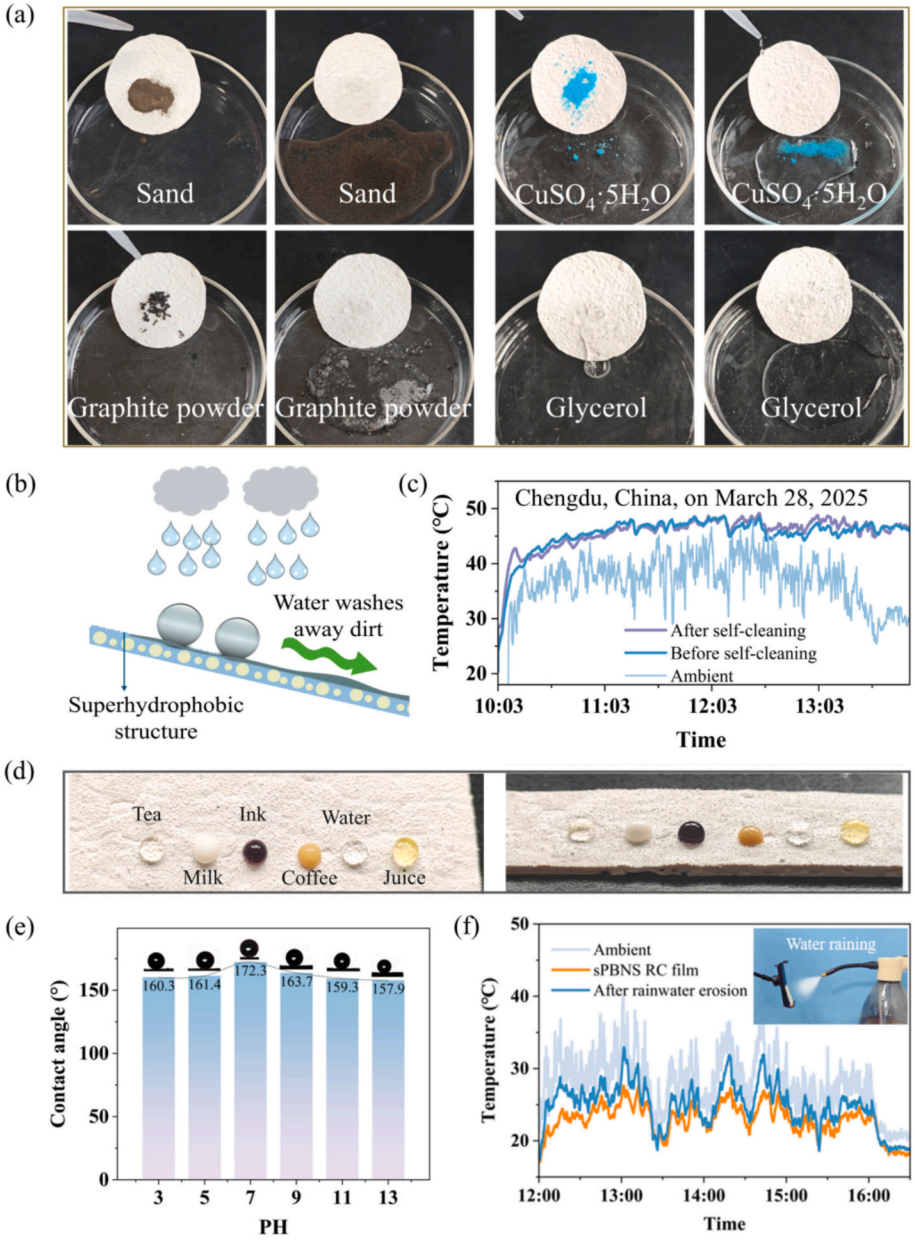

Fig. 7. Self-cleaning performance of the sPBNS RC film. (a) Representative contaminants (sand, $CuSO_4·5H_2O$, graphite powder, glycerol); (b) schematic of water droplets washing away contaminants; (c) cooling performance before and after self-cleaning (Chengdu, China, on March 28, 2025); (d) anti-fouling test; (e) test of acid/alkaline tolerance for solutions of different pH values; (f) rainwater erosion test.

cleaning through water droplet rolling (Fig. 7(b)). This mechanism prevents the accumulation of dust and pollutants on the film surface, thereby avoiding any obstruction of infrared radiation emission and preserving high RC efficiency.

As presented in Fig. 7(c), the outdoor RC performance of the sPBNS RC films before and after self-cleaning tests was evaluated in Chengdu, China, on March 28, 2025. The results show negligible variation in cooling performance after the self-cleaning process, with the cooling performance remaining essentially unchanged compared to the pre-cleaning state. This finding demonstrates that the excellent environmental adaptability and operational stability of the sPBNS RC film for practical outdoor applications. Furthermore, Fig. 7(d) indicates that a range of common liquids (tea, milk, ink, coffee, water, juice) form near-spherical droplets on the film surface, revealing the broad-spectrum liquid repellency and exceptional anti-fouling performance. In addition, the chemical stability of the film was evaluated under acidic and alkaline conditions. Solutions with pH values ranging from 3 to 13 were prepared, and the films were immersed in these solutions for 7 days. Fig. 7(e) shows that the surface contact angle remains at around 160° after immersion in different pH solutions, demonstrating that the as-prepared film has excellent chemical stability. A spray test designed to simulate rainwater erosion was conducted in this study to detest water resistance of the film. An electric spraying device was used to continuously generate fine water mist, allowing the film to keep in a wetted state. Each spraying treatment lasted for 3 h and was repeated for 6 times to simulate long-term rainwater erosion. After the spray treatment, outdoor field performance test was performed on both the sprayed film and the unsprayed film. The results fully demonstrate that the PBNS film can maintain stable radiative cooling performance after multiple water spray treatments, which indicates that the film possesses superior water resistance and environmental stability.

3.7. Mechanical performance

Superhydrophobic coatings are unenviable to suffer from external mechanical abrasion during practical occasions. Therefore, mechanical abrasion durability is becoming a crucial metric for comprehensively evaluating quality of RC films [64]. Fig. 8(a, b) describe that abrasion tests were conducted to assess ability of the sPBNS RC films to resist friction and investigate the effect of abrasion cycles on surface hydrophobicity. It is demonstrated in Fig. 8(c) that the water contact angle slightly decreases with rise of abrasion cycles, which is attributed to mechanical damage to the surface microstructure. The alteration of the surface topography leads to a deterioration in the hydrophobic property. Specifically, the sPBNS RC film retains a high contact angle of 161.7° even after 10 abrasion cycles. This excellent stability is ascribed to the flexibility of the PDMS substrate and the protective role of the h-BN/SiO_2 fillers, which benefits to preserve the surface microstructure during mechanical abrasion.

Fig. 8(d) presents the outdoor temperature curves of the sPBNS RC film before and after mechanical abrasion, measured in Pengzhou on May 20, 2025. The temperature curves before and after abrasion almost overlap, indicating that mechanical abrasion induces no noticeable deterioration in RC performance. This result demonstrates that the sPBNS RC film maintains stable RC capability after repeated friction, confirming its excellent mechanical robustness under practical outdoor conditions. Furthermore, an outdoor field test was conducted (15:30 on June 13, 2025) on the both abraded and unabraded sPBNS RC films. The infrared thermal images in Fig. 8(e) indicate that abrasion resulted in a reduction to cooling performance of the sPBNS RC films, with the abraded film temperature being approximately 4 °C lower than the unabraded film. This is attributed to the wear-induced changes to the

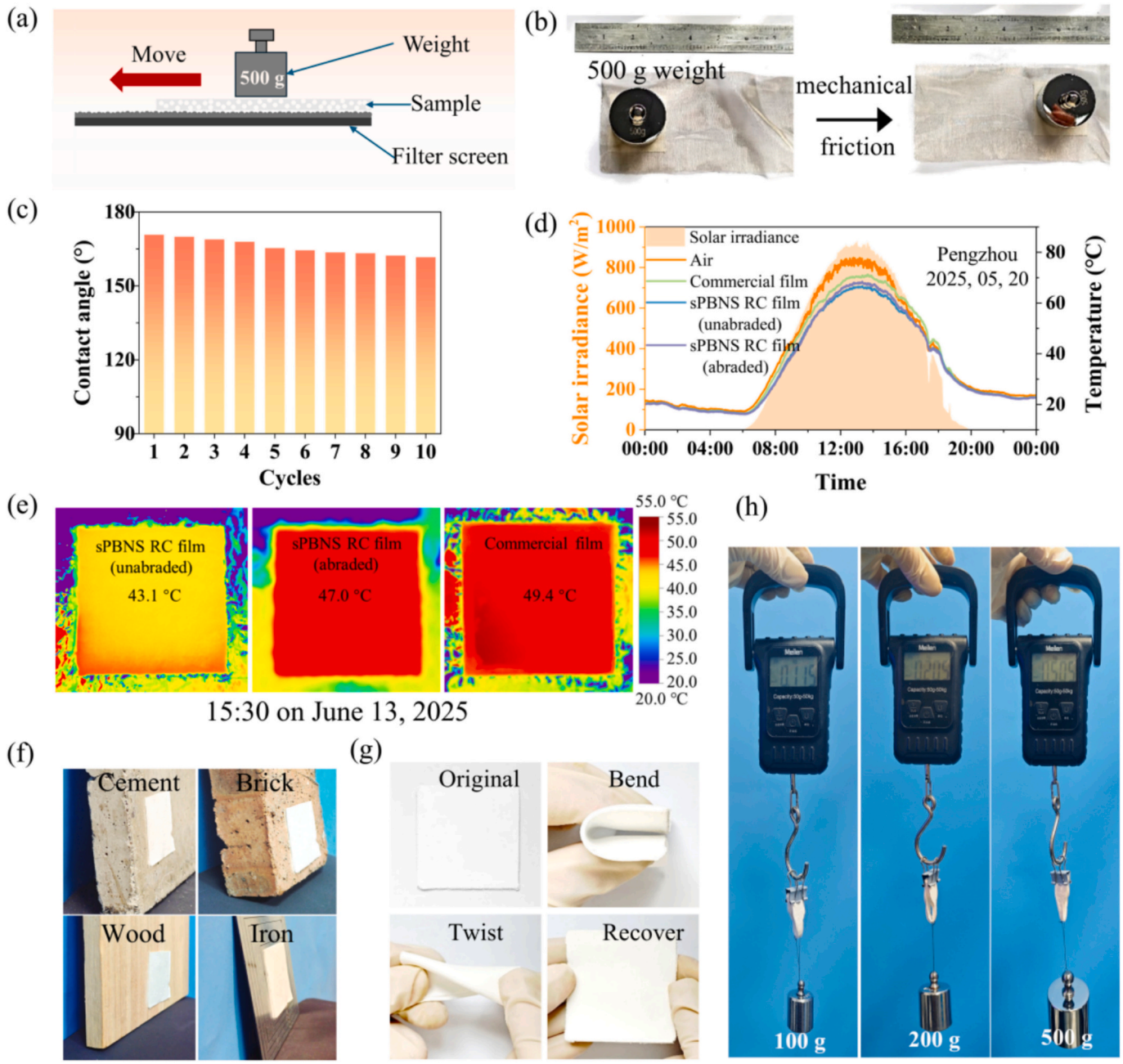

Fig. 8. Mechanical performance of the sPBNS RC film. (a) Schematic of experimental set-up; (b) mechanical friction test; (c) contact angle chart for various frictions; (d) temperature variation of films before and after friction; (e) infrared thermal images; (f) adhesion test; (g) flexibility test; (h) load test.

surface microstructures, and surface roughness is correlated with optical properties [65]. Nevertheless, the RC performance of the abraded sPBNS RC film remains superior to that of the commercial reference film.

Since mechanical stability is critical for the practical deployment of the sPBNS RC film, the mechanical stability of the prepared film was systematically assessed. Fig. 8(f) demonstrates the film can stably adhere to common building materials (cement board, brick, iron plate, wooden board), indicating exceptional adhesion of the as-prepared sPBNS RC film. Fig. 8(g) shows the flexibility test of the sPBNS RC film. After bending and torsional deformation, the PBNS RC film exhibits excellent shape recovery and quickly return to its original morphology. As shown in Fig. 8(h), the load tests indicate that the sPBNS RC film maintains structural ductility without fracture under uniaxial tension of a 500 g load. This robustness is attributed to the synergistic effect of the elastic properties of the PDMS substrate and the filling effect of inorganic fillers. The findings fully confirm that the sPBNS RC film has capacity of high mechanical stability, enabling to obtains considerable potential for long-term real-world applications.

4. Conclusions

This study develops a novel PDMS based RC composite film, incorporating h-BN and SiO_2 as dual functional fillers to simultaneously realize excellent passive cooling and superhydrophobicity. The film is experimentally fabricated through an integrated tape casting-spraying method. Systematic investigations are conducted on structural properties, heat dissipation, self-cleaning and mechanical performance of the as-prepared PDMS-based RC films. Compared with recently reported radiative cooling materials, such as cooling textiles, photonic structures, and cellulose-based films, which often involve trade-offs in durability, fabrication complexity, and environmental stability, the sPBNS RC film developed in this work integrates broadband solar reflectance, strong mid-infrared emissivity, durable hydrophobicity, mechanical flexibility, and environmental stability. This paper provides a technically feasible and cost-effective strategy to optimal design of novel PDMS-based RC composite films, with noticeable dual-enhanced functions of passive cooling and self-cleaning for practical applications. The following findings can be drawn from this investigation:

(1) The enhanced RC performance stems from the synergistic effect between high solar reflectance of h-BN and high infrared emissivity of SiO_2. Their spectrum modulation can be adjusted by the h-BN/SiO_2 loading, spraying amount and film thickness, yields a solar reflectance of 93.2% and an infrared emissivity of 92.3%.
(2) Outdoor field test demonstrates that the PDMS-based RC film can generate a maximum sub-ambient temperature drop of 19.4 °C compared to the air temperature. Theoretical cooling power of the sPBNS RC film can reach up to 85.3 W/m^2 and 153.0 W/m^2 in the daytime and nighttime.
(3) The rough surface structure and embedded hydrophobic particles well guarantees self-cleaning capacity of the sPBNS RC film, with a maximum contact angle of 172.3° and a roll-off angle of 8°. It also maintains outstanding long-term adaptability, mechanical abrasion resistance under various environmental scenarios.

CRediT authorship contribution statement

Xinyu Chen: Writing – original draft, Investigation, Formal analysis, Validation. **Qingyun Zhao:** Conceptualization, Methodology. **Nan Zhang:** Methodology, Resources. **Yanping Yuan:** Resources, Supervision. **Shady Attia:** Conceptualization, Resources. **Zhaoli Zhang:** Writing – original draft, Supervision, Resources, Conceptualization, Methodology.

Declaration of competing interest

The authors declare that they have no known competing financial interests or personal relationships that could have appeared to influence the work reported in this paper.

Acknowledgments

The work is supported by the National Natural Science Foundation of China (No: 52378111 and 52311530700) and Fundamental Research Funds for the Central Universities (No.: 2682024CX104 and 2682024GF021).

Data availability

Data will be made available on request.

References

[1] V. Gupta, C. Deb, Envelope design for low-energy buildings in the tropics: a review, Renew. Sust. Energ. Rev. 186 (2023) 113650, https://doi.org/10.1016/j.rser.2023.113650.
[2] M. Khan, M. Ibrahim, T. Saeed, Space cooling achievement by using lower electricity in hot months through introducing PCM-enhanced buildings, J. Build. Eng. 53 (2022) 104506, https://doi.org/10.1016/j.jobe.2022.104506.
[3] C. Chiatti, F. Marchini, C. Fabiani, I. Kousis, L. Carlosena, A.L. Pisello, Harnessing the potential of radiative cooling for the built environment: a new comprehensive protocol for materials' characterization, Sol. Energy Mater. Sol. Cells 277 (2024) 113074, https://doi.org/10.1016/j.solmat.2024.113074.
[4] C. Deng, B. Zhao, L. Wang, Z. Wang, T. Zhang, F. Qiu, Controllable preparation of wollastonite-based composite coating for highly-efficient passive daytime radiative cooling in building, Sol. Energy 274 (2024) 112586, https://doi.org/10.1016/j.solener.2024.112586.
[5] X. Jiang, Z. Li, J. Du, Y. Jiang, J. Wang, C. Xu, Biomimetic superhydrophobic cotton fabrics with multistage micro-nanostructures for long-term passive radiative cooling, Prog. Org. Coat. 213 (2026) 109966, https://doi.org/10.1016/j.porgcoat.2026.109966.
[6] W. Liu, Q. Tian, Y. Wang, L. Yang, D. Lu, Z. Yao, L. Zhang, Sandwich-like composite membrane for advanced radiative cooling applications, Adv. Membr. 5 (2025) 100133, https://doi.org/10.1016/j.advmem.2025.100133.
[7] F. Marchini, R. Bondi, A. Duri, C. Fabiani, L. Latterini, A.L. Pisello, Coupling vanadium oxide and lead-free perovskite for sustainable passive daytime radiative cooling, Renew. Energy 256 (2026) 123755, https://doi.org/10.1016/j.renene.2025.123755.
[8] Y. He, H. Ma, Z. Zhang, X. Tian, S. Zhang, G. Tang, S. Zhao, Y. Yang, X. Zhang, X. Liu, Durable hierarchically porous polyurethane membrane for efficient passive daytime radiative cooling, Prog. Org. Coat. 212 (2026) 109891, https://doi.org/10.1016/j.porgcoat.2025.109891.
[9] N. Li, L. Wei, M. You, M. Chen, H. Li, H. Liu, Z. Fang, H. Bao, Hierarchically structural TiO_2-PVDF fiber film with particle-enhanced spectral performance for radiative sky cooling, Sol. Energy 259 (2023) 41–48, https://doi.org/10.1016/j.solener.2023.05.011.
[10] X. Yang, Y. Yang, Y. Deng, Z. Li, L. Zhang, Q. Wang, R. Lan, H. Yang, Recent advances in polymer-based radiative cooling material: principle, designs and applications, Rev. Mater. Res. 1 (2025) 100043, https://doi.org/10.1016/j.revmat.2025.100043.
[11] V.S. Hiremath, D.M. Reddy, R. Reddy Mutra, A. Sanjeev, T. Dhilipkumar, N. J, Thermal degradation and fire retardant behaviour of natural fibre reinforced polymeric composites- a comprehensive review, J. Mater. Res. Technol. 30 (2024) 4053–4063, https://doi.org/10.1016/j.jmrt.2024.04.085.
[12] N. Xu, J. Wang, Y. Cui, S. Ren, J. Deng, Q. Gou, Z. Chen, K. Wang, Y. Geng, J. Cui, M. Li, Butterfly wing-inspired microstructured film with high reflectivity for efficient passive radiative cooling, Renew. Energy 229 (2024) 120732, https://doi.org/10.1016/j.renene.2024.120732.
[13] M. Choi, J. Seo, S. Yoon, Y. Nam, J. Lee, B.J. Lee, All-day radiative cooling using a grating-patterned PDMS film emitter, Appl. Therm. Eng. 214 (2022) 118771, https://doi.org/10.1016/j.applthermaleng.2022.118771.
[14] J. Zhang, X. Yang, R. Xu, S. Li, G. Qi, X. Tan, An environmentally friendly porous PDMS film via a template method based for passive daytime radiative cooling, Mater. Lett. 357 (2024) 135686, https://doi.org/10.1016/j.matlet.2023.135686.
[15] R.-R. Gao, C.-H. Xue, X.-J. Guo, H.-D. Wang, M.-C. Huang, C.-Q. Ma, B.-Y. Liu, S.-Q. Lyu, W.-M. Zhang, F.-Q. Deng, J. Cheng, J. Li, H.-W. Wang, Solvent-free fabrication of flexible and mechanically durable superhydrophobic polydimethylsiloxane-based film for sustainable daytime radiative cooling, Opt. Mater. 160 (2025) 116773, https://doi.org/10.1016/j.optmat.2025.116773.
[16] A. Srinivasan, B. Czapla, J. Mayo, A. Narayanaswamy, Infrared dielectric function of polydimethylsiloxane and selective emission behavior, Appl. Phys. Lett. 109 (2016) 061905, https://doi.org/10.1063/1.4961051.

[17] C. Fan, H. Xie, J. Wang, Realization of bifunctional photothermal and radiative cooling based on self-adaptive VO_2/PDMS metamaterial, Sol. Energy 266 (2023) 112192, https://doi.org/10.1016/j.solener.2023.112192.
[18] S. Zhang, Z. Wu, Z. Liu, H. Lin, Z. Lin, J. Li, S. Kong, Z. Hu, Cost effective 24-h radiative cooler with multiphase interface enhanced solar scattering and thermal emission, Mater. Today Commun. 31 (2022) 103398, https://doi.org/10.1016/j.mtcomm.2022.103398.
[19] Y. Liu, Y. Tian, X. Liu, F. Chen, A. Caratenuto, Y. Zheng, Intelligent regulation of VO_2-PDMS-driven radiative cooling, Appl. Phys. Lett. 120 (2022) 171704, https://doi.org/10.1063/5.0089353.
[20] S. Kim, S. Lee, J. Lee, H.W. Choi, W. Choi, Y.T. Kang, Passive isothermal film with self-switchable radiative cooling-driven water sorption layer for arid climate applications, Nat. Commun. 15 (2024) 8000, https://doi.org/10.1038/s41467-024-52328-z.
[21] Y. Guo, Three-layered films enable efficient passive radiation cooling of buildings, E-Polymers 24 (2024) 20240071, https://doi.org/10.1515/epoly-2024-0071.
[22] J. Sun, J. Wang, T. Guo, H. Bao, S. Bai, Daytime passive radiative cooling materials based on disordered media: a review, Sol. Energy Mater. Sol. Cells 236 (2022) 111492, https://doi.org/10.1016/j.solmat.2021.111492.
[23] Z. Guo, I. Katsamba, D. Carne, D. Feng, K. Moss, E. Barber, Z. Fang, A. Felicelli, X. Ruan, Electronic and phononic characteristics of high-performance radiative cooling pigments h-BN: A comparative study to $BaSO_4$, Mater. Today Phys. 54 (2025) 101721, https://doi.org/10.1016/j.mtphys.2025.101721.
[24] G.R. Pisharody, P. Sahoo, D.S. Shankar Rao, H.S.S. Ramakrishna Matte, D. Sikdar, S. Krishna Prasad, IR regulation through preferential placement of h-BN nanosheets in a polymer network liquid crystal, Mater. Horiz. 11 (2024) 554–565, https://doi.org/10.1039/D3MH01467C.
[25] J. Yan, M. Han, L. Zhu, X. Zhang, M. Xu, M. She, Y. Cai, X. Liu, H. Wang, S. Xiong, L. Wang, Bionic hierarchical metalized thermally responsive dynamic daytime passive radiative cooling nanocomposites, Compos. Sci. Technol. 250 (2024) 110518, https://doi.org/10.1016/j.compscitech.2024.110518.
[26] W. Zhang, Y. Wang, H. Sun, C. Liu, C. Shen, X. Liu, Thermal conductive high-density polyethylene/boron nitride composites with high solar reflectivity for radiative cooling, Adv. Compos. Hybrid Mater. 6 (2023) 163, https://doi.org/10.1007/s42114-023-00739-9.
[27] R.A. Yalçın, E. Blandre, K. Joulain, J. Drévillon, Daytime radiative cooling with silica fiber network, Sol. Energy Mater. Sol. Cells 206 (2020) 110320, https://doi.org/10.1016/j.solmat.2019.110320.
[28] Y. Zhang, J. Yu, In situ formation of SiO_2 nanospheres on common fabrics for broadband radiative cooling, ACS Appl. Nano Mater. 4 (2021) 11260–11268, https://doi.org/10.1021/acsanm.1c02841.
[29] C. Lin, K. Wang, Y. Shi, T. Li, Z. Liu, Z. Mao, Synergistic hierarchical porosity and TiO_2 scattering in liquid-induced phase separation fabricated coatings for radiative cooling and enhanced stability and durability, Sol. Energy Mater. Sol. Cells 296 (2026) 114061, https://doi.org/10.1016/j.solmat.2025.114061.
[30] Y. Zhang, X. Tan, G. Qi, X. Yang, D. Hu, P. Fyffe, X. Chen, Effective radiative cooling with ZrO_2/PDMS reflective coating, Sol. Energy Mater. Sol. Cells 229 (2021) 111129, https://doi.org/10.1016/j.solmat.2021.111129.
[31] Q. Zhang, S. Wang, X. Wang, Y. Jiang, J. Li, W. Xu, B. Zhu, J. Zhu, Recent progress in daytime radiative cooling: advanced material designs and applications, Small Methods 6 (2022) 2101379, https://doi.org/10.1002/smtd.202101379.
[32] H. Bao, C. Yan, B. Wang, X. Fang, C.Y. Zhao, X. Ruan, Double-layer nanoparticle-based coatings for efficient terrestrial radiative cooling, Sol. Energy Mater. Sol. Cells 168 (2017) 78–84, https://doi.org/10.1016/j.solmat.2017.04.020.
[33] M. Feng, Z. Xia, Z. Liu, T. Zhou, H. Sun, X. Liu, Double-layer radiative cooling coating comprising a UV reflective layer and hollow TiO_2, Sol. Energy 302 (2025) 113974, https://doi.org/10.1016/j.solener.2025.113974.
[34] X. Ran, Synergistic radiative-evaporative cooling film for high-efficiency daytime passive cooling and photovoltaic thermal management, J. Mater. Sci. Technol. 249 (2026) 189–195, https://doi.org/10.1016/j.jmst.2025.05.057.
[35] Z. Xia, Passive radiative cooling films doped with SiO_2-TiO_2 of different particle sizes with excellent solar reflectivity and high infrared emissivity, Sol. Energy Mater. Sol. Cells 292 (2025) 113812, https://doi.org/10.1016/j.solmat.2025.113812.
[36] B. Zhang, Self-cleaning and anticorrosive pompon chrysanthemum-like hollow silica nanosphere@boron nitride nanosheets hierarchical coating for highly efficient daytime passive radiative cooling, Sol. Energy Mater. Sol. Cells 282 (2025) 113429, https://doi.org/10.1016/j.solmat.2025.113429.
[37] J. Li, R. Wang, M. Xing, R. Wang, Effect of random microstructure of the film surface on daytime radiative cooling performance, Sol. Energy 292 (2025) 113434, https://doi.org/10.1016/j.solener.2025.113434.
[38] P. Chen, G. Wang, J. Li, M. Zhang, X. Qiao, Preparation of textured epoxy resin coatings for excellent hydrophobicity and corrosion resistance, Prog. Org. Coat. 175 (2023) 107312, https://doi.org/10.1016/j.porgcoat.2022.107312.
[39] B. Zhao, R. Jia, Preparation of super-hydrophobic films based on waterborne polyurethane and their hydrophobicity characteristics, Prog. Org. Coat. 135 (2019) 440–448, https://doi.org/10.1016/j.porgcoat.2019.06.025.
[40] L. Li, X. Li, J. Chen, L. Liu, J. Lei, N. Li, G. Liu, F. Pan, One-step spraying method to construct superhydrophobic magnesium surface with extraordinary robustness and multi-functions, J. Magnesium Alloys 9 (2021) 668–675, https://doi.org/10.1016/j.jma.2020.06.017.
[41] X. Zhao, Y. Fang, Structural colored fabric with superhydrophobicity by assembly SiO_2@PPy composite microspheres and spraying PDMS on white fabric, Opt. Mater. 161 (2025) 116826, https://doi.org/10.1016/j.optmat.2025.116826.
[42] S. He, J. Chen, Y. Lu, S. Huang, K. Feng, Enhanced waterproof performance of superhydrophobic SiO_2/PDMS coating, Prog. Org. Coat. 197 (2024) 108845, https://doi.org/10.1016/j.porgcoat.2024.108845.
[43] F. Xu, F. Wang, J. Ou, Superhydrophobic polytetrafluoroethylene/polyvinylidene fluoride coating for passive daytime radiative refrigeration, Colloids Surf. A Physicochem. Eng. Asp. 676 (2023) 132121, https://doi.org/10.1016/j.colsurfa.2023.132121.
[44] P. Li, A. Wang, J. Fan, Q. Kang, P. Jiang, H. Bao, X. Huang, Thermo-optically designed scalable photonic films with high thermal conductivity for subambient and above-ambient radiative cooling, Adv. Funct. Mater. 32 (2022) 2109542, https://doi.org/10.1002/adfm.202109542.
[45] Y. Fu, L. Chen, Y. Guo, Y. Shi, Y. Liu, Y. Zeng, Y. Lin, D. Luo, Pyramid textured photonic films with high-refractive index fillers for efficient radiative cooling, Adv. Sci. 11 (2024) 2404900, https://doi.org/10.1002/advs.202404900.
[46] A. Choudhury, A.K. Bhowmick, C. Ong, M. Soddemann, Effect of various nanofillers on thermal stability and degradation kinetics of polymer nanocomposites, J. Nanosci. Nanotechnol. 10 (2010) 5056–5071, https://doi.org/10.1166/jnn.2010.3030.
[47] A. Camposeo, A. Arkadii, L. Romano, F. D'Elia, F. Fabbri, E. Zussman, D. Pisignano, Impact of size effects on photopolymerization and its optical monitoring in-situ, Addit. Manuf. 58 (2022) 103020, https://doi.org/10.1016/j.addma.2022.103020.
[48] A. Shrivastava, S. Saini, S. Singh, Ab-initio investigations of electronic and optical properties of Sn-hBN hetero-structure, Phys. B Condens. Matter 624 (2022) 413390, https://doi.org/10.1016/j.physb.2021.413390.
[49] Q. Pan, M. Wang, Z. Huang, X. Qiu, Y. Wang, F. Zhao, M. Zhu, X. Guo, C. Chen, S. Zhang, J. Wang, Z. He, S. Yu, Biomimetic pyramid structure film for enhancing building radiative cooling, Adv. Sci. 12 (2025) 2413559, https://doi.org/10.1002/advs.202413559.
[50] H. Liu, X. Yang, L. Wang, C. Jiang, D. Liu, Y. Ji, F. Zhang, D. Chen, Gaussian oscillator model of the dielectric constant of SiO2 thin film in infrared range, Acta Phys. Sin. 66 (2017) 054211, https://doi.org/10.7498/aps.66.054211.
[51] C. Wu, Large-roll growth of 25-inch hexagonal BN monolayer film for self-release buffer layer of free-standing GaN wafer, Sci. Rep. 6 (2016) 34766, https://doi.org/10.1038/srep34766.
[52] J. Huang, H. Tian, H. Zhang, Z. Zhu, S. Qin, W. Xu, J. Wan, Two-dimensional materials for enhanced mid-infrared thermal management, 2D Mater. 12 (2025) 032003, https://doi.org/10.1088/2053-1583/addad4.
[53] H. Cho, D. Lee, S. Hong, H. Kim, K. Jo, C. Kim, I. Yoon, Surface modification of ZrO_2 nanoparticles with TEOS to prepare transparent ZrO_2@SiO_2-PDMS nanocomposite films with adjustable refractive indices, Nanomaterials 12 (2022) 2328, https://doi.org/10.3390/nano12142328.
[54] H. Liu, Y. Sun, J. Ren, D. Liang, Y. Yang, Z. Fan, C. Wang, Inorganic multilayer film with high infrared selective emission enhanced by SiN_x for daytime radiative cooling, ACS Appl. Energy Mater. 7 (2024) 2478–2486, https://doi.org/10.1021/acsaem.4c00006.
[55] M. Chen, D. Pang, X. Chen, H. Yan, Investigating the effective radiative cooling performance of random dielectric microsphere coatings, Int. J. Heat Mass Transf. 173 (2021) 121263, https://doi.org/10.1016/j.ijheatmasstransfer.2021.121263.
[56] X. Song, H. Gong, H. Li, M. Zhang, L. Jiang, C. Wang, P. Jiang, H. Wang, K. Cao, G. Liu, Q. Zhao, T. Fan, Improved abrasion-resistant coatings using designed inorganic particles for durable radiative cooling, Sol. Energy Mater. Sol. Cells 275 (2024) 113003, https://doi.org/10.1016/j.solmat.2024.113003.
[57] H. Zhang, Y. Cai, L. Liu, J. Qin, Y. Li, Z. Yang, Z. Sun, R. Wang, Y. Zhang, Y. Feng, Z. He, W. Zhang, C. Feng, X. Xue, Superamphiphobic coatings with subambient daytime radiative cooling—part 1: optical and self-cleaning features, Sol. Energy Mater. Sol. Cells 245 (2022) 111859, https://doi.org/10.1016/j.solmat.2022.111859.
[58] K. Alam, S. Ali, A. Saboor, M. Salman, Maoz, M. Humayun, M. Sadiq, M. Arif, Antireflection, superhydrophilic nano-porous SiO2 coating based on aerosol impact spray deposition technique for solar PV module, Coatings 9 (2019) 497, https://doi.org/10.3390/coatings9080497.
[59] C. Feng, Y. Lei, X. Huang, W. Zhang, Y. Feng, X. Zheng, Experimental and theoretical analysis of sub-ambient cooling with longwave radiative coating, Renew. Energy 193 (2022) 634–644, https://doi.org/10.1016/j.renene.2022.05.037.
[60] X.-Y. Xu, H. Zhang, X.-J. Kang, Y.-Z. Zhang, C.-Y. He, X.-H. Gao, High-performance, superhydrophobic, durable photonic structure coating for efficient passive daytime radiative cooling, Mater. Today Phys. 48 (2024) 101556, https://doi.org/10.1016/j.mtphys.2024.101556.
[61] Y. Dong, H. Han, F. Wang, Y. Zhang, Z. Cheng, X. Shi, Y. Yan, A low-cost sustainable coating: improving passive daytime radiative cooling performance using the spectral band complementarity method, Renew. Energy 192 (2022) 606–616, https://doi.org/10.1016/j.renene.2022.04.093.
[62] R. Liu, S. Wang, Z. Zhou, K. Zhang, G. Wang, C. Chen, Y. Long, Materials in radiative cooling technologies, Adv. Mater. 37 (2025) 2401577, https://doi.org/10.1002/adma.202401577.
[63] R. Tan, H. Zhang, L. Wang, Y. Li, P. Xue, S. Xu, G. Bai, Hierarchically structured superhydrophobic composite films for efficient radiative cooling and energy saving, J. Mater. Chem. A 13 (2025) 15941–15950, https://doi.org/10.1039/D5TA01065A.
[64] Z. Huang, S. Zhu, M. Zhu, Y. Tian, L. Ma, A durable superhydrophobic surface with bud-particle structure prepared by one-step spray method, Appl. Surf. Sci. 679 (2025) 161255, https://doi.org/10.1016/j.apsusc.2024.161255.
[65] A. Larena, F. Millán, G. Pérez, G. Pinto, Effect of surface roughness on the optical properties of multilayer polymer films, Appl. Surf. Sci. 187 (2002) 339–346, https://doi.org/10.1016/S0169-4332(01)01044-3.